Flow noise estimation models for axial flow past towed sonar arrays

Rakesh Sekharipuram Sekar
Department of Mechanical Engineering,
Indian Institute of Technology Palakkad,
Palakkad, Kerala, 678003, India
Email: 132203001@smail.iitpkd.ac.in

Senthil Rajan S
Naval Physical Oceanographic Laboratory,
Ernakulam, Kerala, 682021, India
Email: senthilrajan.npol@gov.in

Anoop Akkoorath Mana*
Department of Mechanical Engineering,
Indian Institute of Technology Palakkad,
Palakkad, Kerala, 678003, India
Email: akkoorath@iitpkd.ac.in

ABSTRACT

Towed sonar arrays house a series of pressure sensors inside a fluid-filled elastic tube. Towing of the sonar array in water generates a turbulent boundary layer on the exterior surface of the elastic tube. The pressure fluctuations in the turbulent boundary layer along with other ambient pressure fluctuations, excites the elastic tube and further generates pressure disturbances in the interior fluid. In this work, a new semi-empirical model of the turbulent pressure spectrum is presented. The new model predictions show a closer agreement with the available experimental results at all tow speeds. A three-dimensional vibroacoustic model of the fluid-filled elastic tube is also presented in this work. The vibroacoustic model is fully coupled and considers both breathing mode and first order variations in the elastic tube and the acoustic field variables. Further, the turbulent pressure spectrum semi-empirical model and the three-dimensional vibroacoustic model are used to compute

*Address all correspondence for other issues to this author.

the on-axis sound pressure level due to the external turbulent pressure excitation at different elastic tube diameters and tow speeds. At low frequencies, increasing tube diameter has little effect on flow noise, while at higher frequencies, flow noise decreases with larger diameters. Increasing tow speed raises flow noise across all frequencies.

INTRODUCTION

Towed sonar arrays contain a series of pressure sensors enclosed within a fluid-filled elastic tube. As the sonar array is towed through the water, a thick layer of turbulent flow is generated over the exterior surface of the tube. The pressure fluctuations in this turbulent boundary layer (TBL), along with other ambient sea pressure variations, excite the elastic tube and subsequently produce acoustic pressure disturbances within the interior fluid. The hydrophones placed in the interior fluid picks these acoustic signals. The signals associated with the turbulent pressure fluctuations are called flow noise. Currently, the flow noise is measured either by towing the sonar array in open water using a dinghy or by allowing the hydrophone to free fall in water [1]. In the first case, noise from the boat and vibrations of the towline connections pollute the measured acoustic signals [2]; whereas in the second case, the useful measurements can be made only at the terminal velocity of the hydrophone. This work aims at developing a fully-coupled vibroacoustic model for predicting the flow noise in towed sonar arrays which is useful over wide range of towing speeds and tube diameters.

A widely used model for predicting the turbulent pressure spectrum is that developed by Corcos [3] for the flow over a flat plate. In this model, the turbulent pressure is varying exponentially with respect to both the axes of the flat plate. Although this model is widely used in engineering applications, it has a major shortcoming that it is overestimating the pressure level at low wavenumbers. Chase [4] presented a simpler turbulent pressure spectrum model for the flow over a flat plate. The model is based on experimental observations and uses direct dependence on the flow and dimensional parameters. Frendi and Zhang [5] analysed the Corcos [3] model and proposed a turbulent model for the flow over a flat plate based on large eddy simulation (LES) and direct numerical simulation (DNS) computational results. Frendi's model involves the use of an auto spectrum which was derived by Goody [6]. The Frendi model predictions are found to match well with an earlier experimental result on flow over a flat plate. Some of the observations of the Chase and Frendi models are relevant to the present work and are discussed in section 1. Francis *et al*. [7] used LES and Reynolds averaged Navier Stokes (RANS) computational method to study the wavenumber frequency spectrum of the turbulent pressure field over a flat plate. This work presents an exhaustive discussion on similar problems in the literature.

Chase [4] developed a model for computing the turbulent pressure spectrum for an axial flow past a cylinder by modifying his earlier flat plate model. While modifying, Chase considered the radius of the cylinder as one of the parameters instead of the length of the flat plate. Chase derived azimuthal harmonic spectral density by integrating the turbulent pressure spectrum of the flat plate in the cross-flow direction. The details of this model are presented in section 1.1.

Carpenter and Kewley [8] conducted experiments for finding the flow noise inside a fluid-filled elastic tube while towed behind a ship and compared the results with that predicted by Chase [4]. The authors also proposed a tube transfer function for computing the flow noise inside the tube. Knight [9] performed similar analytical simulations as in [8] but with different types of hydrophones and compared the flow noise with that for an ideal hydrophone. The ideal hydrophone was assumed to have unit acoustic response and zero convective response. Knight also used an approximate tube transfer function to find the noise inside the fluid-filled elastic tube.

Unnikrishnan *et al*. [2] performed experiments to measure the turbulent pressure field outside the elastic tube by towing the sonar array in a quiet lake at different speeds. The work presents a comparison of the experimental results with the available semi-empirical model predictions. It was found that the semi-empirical model estimations match with the measurements only at high tow speeds. Karthik *et al*. [10] studied the turbulent pressure spectrum over a cylinder with the help of an LES computational model. The model predictions match well with the experimental results of Unnikrishnan *et al*. [2]. Karthik *et al*. also presented a non-dimensional turbulent flow noise spectrum for easy estimation of the spectrum at different tow speeds and tube diameters.

Both Carpenter and Kewley [8] and Knight [9] estimated the flow noise inside a fluid-filled elastic tube with the help of the Chase model for the turbulent pressure spectrum and an approximate tube transfer function. Jineesh and Ebenezer [11] developed a better axisymmetric model of the fluid-filled elastic tube and used it to estimate the flow noise inside the tube. It was found that the earlier approximate transfer function model overestimated the flow noise inside the tube.

This paper develops a new semi-empirical model of the turbulent pressure spectrum for axial flow past a solid cylinder. It also presents a fully coupled three-dimensional vibroacoustic model of a fluid-filled elastic tube. Furthermore, these two models are used to compute the on-axis sound pressure level resulting from an external turbulent pressure excitation on the elastic tube. This paper is organized as follows: Section 1 discusses two existing semi-empirical models for estimating turbulent pressure spectrum for axial flow past a solid cylinder. Section 2 discusses the development of a new semi-empirical model for the turbulent pressure spectrum, which provides improved predictions compared to existing models. Section 3 discusses the development of a three-dimensional vibroacoustic model for estimating the on-axis flow noise inside a fluid-filled elastic tube. Further, Section 4 presents the results on interior acoustic pressure spectrum and on-axis flow noise inside a fluid-filled elastic tube and are compared with the available results in the literature.

1 REVIEW OF SEMI-EMPIRICAL MODELS OF TURBULENT PRESSURE SPECTRUM

One of the objective of this study is to predict the flow noise resulting from turbulent boundary layer excitation. To achieve this, a semi-empirical model that can estimate the turbulent pressure exerted by fluid flow on a cylindrical tube, is required. Two existing semi-empirical models for turbulent pressure fluctuation are discussed in this section. Further, flow noise at the outer surface of the tube is estimated using these models, showing its variation in comparison to available experimental results [2].

1.1 Chase model

Chase [4] proposed a semi-empirical model for predicting the frequency-wavenumber spectrum of turbulent pressure field over a solid cylinder and is given by

$$\hat{p}_0(k_z,\omega) = C\rho^2\nu_*^3R^2\left[(k_zR)^2+\frac{1}{12}\right]\times\left[\frac{(\omega R-u_ck_zR)^2}{h^2\nu_*^2}+(k_zR)^2+b_1^{-2}\right]^{-2.5}. \quad (1)$$

The important parameters in the above equation are axial wavenumber k_z, frequency ω, density of the fluid ρ, convective speed u_c ($= 0.68u$, where u is the tow speed), $C = 0.063$, $h = 3.7$, $\nu_* = 0.04U$ and tube radius R [4, 8, 9, 12, 13].

1.2 Frendi model

Frendi's model for the turbulent pressure spectrum for a flat plate is given by [5]

$$\hat{R}(k_z,k_2,\omega) = C_1R^*(\omega)e^{-\hat{\alpha}r_k}. \quad (2)$$

In the above equation, C_1 is given by

$$C_1 = \alpha^2m\delta^2\frac{1}{2\pi}, \quad (3)$$

where α can be computed using

$$\alpha = \frac{a_1}{\pi}\frac{1}{\sqrt{1+a_2(\frac{\omega\delta}{u_t}-50)^2}}. \quad (4)$$

In the above equation, $a_1 = 4.7$, $a_2 = 3 \times 10^{-5}$ [5], u_t is the friction velocity (=0.04u, a small fraction of tow velocity u) and δ is the boundary layer thickness [14] given by

$$\delta = [48 Re_a^{-1} Re_x^{(0.0226 \log Re_a + 0.2478)}]^{\frac{1}{0.91}}. \tag{5}$$

In the above equation, Re_a is the radius based Reynold's number ($\frac{\rho u R}{\mu}$) and Re_x is length based Reynold's number ($\frac{\rho u x}{\mu}$), x is distance of a point on the cylinder from the leading edge and μ is the dynamic viscosity of the fluid medium. The constant m in Eq. (3) is a scaling factor which is approximately taken as 1/7.7 [5].

$R^*(\omega)$ in Eq. (2) is the auto-spectrum given by [6]

$$R^*(\omega) = \frac{3\tau_w^2 \omega^2 (\frac{\delta}{u})^3}{[(\frac{\omega\delta}{u})^{0.75} + 0.5]^{3.7} + [1.1 R_t^{-0.57} (\frac{\omega\delta}{u})]^7}. \tag{6}$$

In the above equation, τ_w is the shear stress at the wall, R_t is the ratio of time scale [6] given by

$$R_t = \left(\frac{u_t}{u}\right)\left(\frac{u_t \delta}{\nu}\right), \tag{7}$$

where ν is the kinematic viscosity.

$\hat{\alpha}$ in Eq. (2) is given by $\hat{\alpha} = \alpha\delta$ and r_k depends on the axial and crossflow wavenumbers and is given by

$$|r_k|^2 = \left(k_z - \frac{\omega}{u_c}\right)^2 + (mk_2)^2. \tag{8}$$

In the above equation, k_2 denotes the cross flow wavenumber and u_c is the convective speed (= 0.68u, a large fraction of tow speed u). Eq. (2) can be modified for estimating turbulent pressure spectrum for an axial flow past a solid cylinder as

$$\hat{p}_0(k_z,\omega) = \int_{-1/2R}^{1/2R} \hat{R}(k_z,k_2,\omega)dk_2. \tag{9}$$

The estimation of flow noise using the models discussed in this section and its comparison with the findings of experiments are presented below.

1.3 Flow noise

Here, the estimation of flow noise, as measured by a series of hydrophones placed at the outer surface of a solid cylinder, is discussed and compared with the experimental results [2]. The flow noise associated with the turbulent pressure spectrum $p_0(k_z,\omega)$ as registered by an array of hydrophones is [2]

$$Q(\omega) = \int_{-\infty}^{\infty} \hat{p}_0(k_z,\omega)H(k_z)dk_z. \tag{10}$$

In the above equation, $H(k_z)$ is the hydrophone response function. The hydrophone array is a set of large number of similar elements with specific length arranged at a fixed distance apart. This array acts as noise filter and its response is given by [2]

$$H(k_z) = \frac{sin(k_z dN/2)}{Nsin(k_z d/2)}\frac{sin(lk_z/2)}{lk_z/2}, \tag{11}$$

where N is the number of hydrophone elements in the array, d is the distance between two hydrophones and l is the length of individual hydrophones.

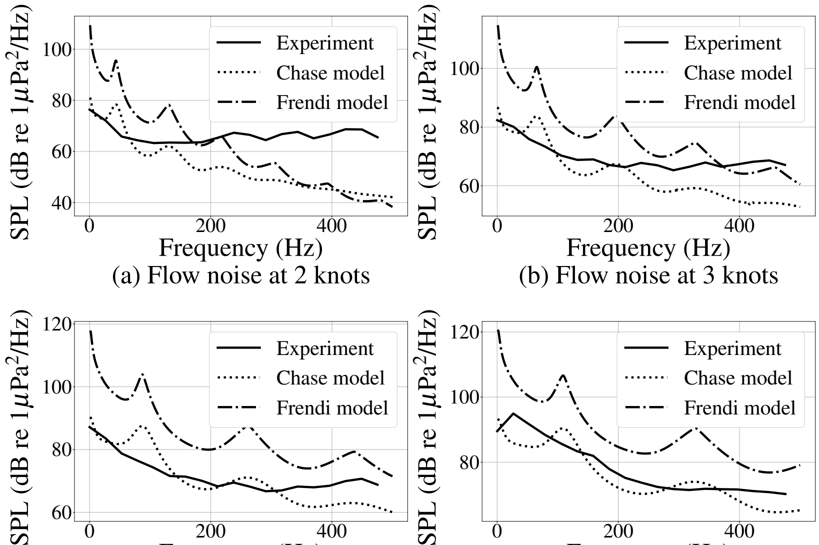

(a) Flow noise at 2 knots
(b) Flow noise at 3 knots
(c) Flow noise at 4 knots
(d) Flow noise at 5 knots

Fig. 1. Comparison of flow noise predicted by Chase [4] and Frendi [5] models with the experimental results [2] at different tow speeds.

The sound pressure level (SPL) associated with the flow noise $Q(\omega)$ is given by

$$SPL = 10\ log_{10}\left(\frac{Q(\omega)}{p_{ref}^2}\right), \tag{12}$$

where $p_{ref} = 1 \times 10^{-6}$ Pa is the reference acoustic pressure in water.

Figure 1 compares the flow noise estimated by the Chase [4] and Frendi [5] models with the experimental results [2] at various tow speeds for a solid cylinder having a diameter of 0.01 m. The sonar array consists of 66 hydrophones, each of length 8 mm, placed at the outer surface of the cylinder with an interval of 16 mm. It is evident from Fig. 1 that the Frendi model consistently overestimates the flow noise at almost all frequencies and tow speeds, whereas the Chase model aligns well with experiments at high tow speeds. However, at low speeds, there is a significant difference between the Chase model and the experiment, especially at high frequencies. Regardless of tow speed, both models predict a significant reduction in flow noise with frequency compared to the experimental results. To address these differences, a new model of the turbulent pressure spectrum is proposed in this work to better match the experimental data, particularly at low tow speeds. The development of this new model is discussed in the following section.

2 A NEW SEMI-EMPIRICAL MODEL OF THE TURBULENT PRESSURE SPECTRUM

It is shown in the previous sections that the Chase and Frendi models show a significant deviation from the experimental results [2] at low tow speeds and at high frequencies. In this section, a new semi-empirical model of the turbulent pressure spectrum is developed that closely aligns with the experimental results [2]. This new model is derived using the insights from both the Chase and Frendi models and is referred to as the *hybrid model*.

2.1 The hybrid model

In the *hybrid model*, the pressure spectrum of the Chase model [4] (Section 1.1) is used in conjunction with the exponential decay function present in the Frendi model [5] (Section 1.2). Accordingly, the turbulent pressure spectrum is given by

$$\hat{p}(k_z, k_2, \omega) = C_3 \bar{P}(\omega) e^{-\hat{\alpha} r_k}. \tag{13}$$

In the above equation, the autospectrum $\bar{P}(\omega)$ is given by

$$\bar{P}(\omega) = \int_{-\infty}^{\infty} \hat{p}_0(\omega, k_z) dk_z, \tag{14}$$

where $\hat{p}_0(\omega, k_z)$ is the same as that used in the Chase model (Eq. (1)). In this new model, the wavenumber dependency is included in the form of an exponential function $e^{-\hat{\alpha} r_k}$, where $\hat{\alpha} = \alpha\delta$ with

$$\alpha = \frac{a_1}{\pi} \frac{1}{\sqrt{1 + a_2(\frac{\omega\delta}{u_t} - 50)^2}}, \tag{15}$$

$$\delta = [48 Re_a^{-1} Re_x^{(0.0226 \log Re_a + 0.2478)}]^{\frac{1}{0.91}} \tag{16}$$

and

$$|r_k|^2 = \left(k_z - \frac{\omega}{u_c}\right)^2 + (mk_2)^2. \tag{17}$$

In Eq. (15), a_1 and a_2 determine the behavior of the spectrum at low and high frequencies, respectively. It has been observed in Fig. 1 that the predictions of the Frendi model deviate more at higher frequency ranges. Therefore, the value of a_2 is decreased from 3×10^{-5} to 3×10^{-6}. Different values of a_1 and C_3 were tested to match the experimental results given in Fig. 1. A better match is found with the experimental data when $a_1 = 1$ and $C_3 = 1 \times 10^{-4}$. Furthermore, the turbulent pressure spectrum given in Eq. (13) is integrated over the cross-flow wavenumber k_2 from $-1/2R$ to $1/2R$ to obtain the pressure spectrum $\hat{p}_0(k_z, \omega)$ for the axial flow past a solid cylinder [4]. Thus,

$$\hat{p}_0(k_z, \omega) = \int_{-1/2R}^{1/2R} \hat{p}(k_z, k_2, \omega) dk_2. \tag{18}$$

The hybrid model is used to compute the flow noise for axial flow past a solid cylinder. The results of the new model and their comparison with the existing models and Unnikrishnan's experimental results [2] are presented in the next subsection.

2.2 Flow noise

The flow noise can be computed using Eq. (10). Here, the turbulent pressure spectrum $\hat{p}_0(k_z, \omega)$ for the new hybrid model is given by Eq. (18) and the hydrophone response function $H(k_z)$ is given by Eq. (11). A comparison of flow noise measured in SPL (see Eq. (12)) computed using the new hybrid model, Chase model [4] and Unnikrishnan's experiment [2] are shown in Fig. 2. It can be seen that the predictions of the new hybrid model are consistent with the mea-

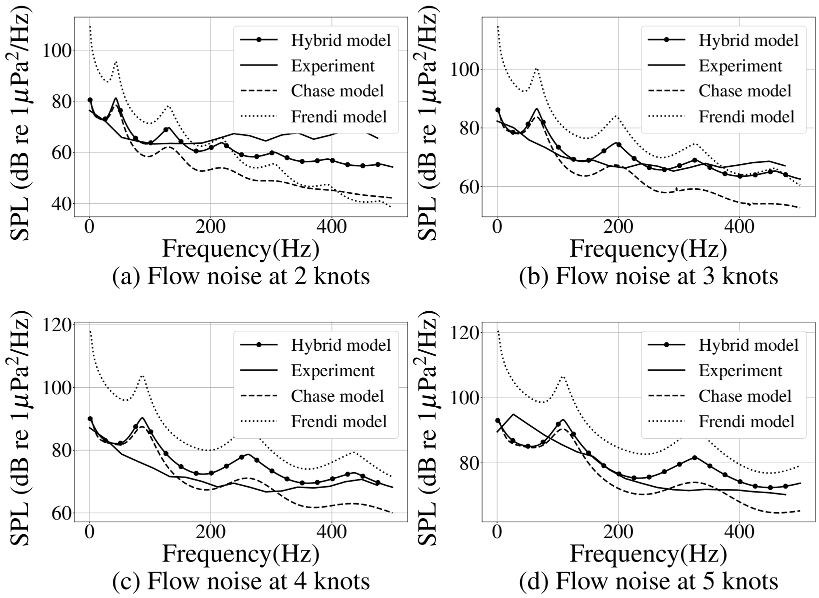

Fig. 2. A comparison of flow noise predicted by the hybrid model, the Chase model [4] and Frendi model [5] with that measured from experiments [2] at different tow speeds.

sured values [2] at all frequencies and towing speeds. Although the hybrid model underpredicts noise at high frequencies for the 2 knots case, the predictions are better than that by the existing Chase and Frendi models.

A comparison of the turbulent pressure spectrum $\hat{p}_0(k_z, \omega)$ predicted by the hybrid model (Eqs. (13)-(18)), the Chase model (Eq. (1)) and the Frendi model (Eq. (9)) for different frequencies at 2 knots is shown in Fig. 3. Here, the diameter of the cylinder is chosen as 10 mm, density of the fluid is 1000 kg/m^3 and the SPL is calculated at 11 m from the leading edge of the solid cylinder. It can be seen from Fig. 3 that for a given frequency, at low wavenumbers, the turbulent pressure spectrum increases at a slow rate. It peaks at convective wavenumber k_c $(= \omega/u_c)$ forming a convective ridge. It can be seen that while all the models predict a 'flat' spectrum at lower wavenumbers and a ridge at convective wavenumber, their predictions differ significantly at large wavenumbers. The presence of an exponential function results in an exponential decrease in the spectrum at large wavenumbers for the hybrid and Frendi models. Chase model predicts a higher spectrum with a smaller slope at large wavenumbers. It can be seen from Fig. 3 that the predictions by the three models are closer at lower frequencies. However, at high frequencies,

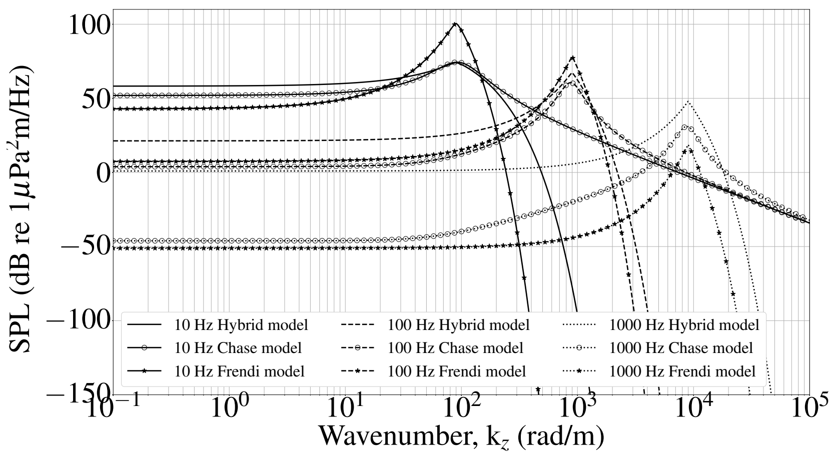

Fig. 3. A comparison of the turbulent pressure spectrum $\hat{p}_0(k_z, \omega)$ given by the hybrid model (Eq. (18)), Chase (Eq. (1)) and Frendi (Eq. (9)) model at 2 knots.

182 the hybrid model predicts a spectrum that is higher than the rest. This difference in the spectrum
183 predicted by the hybrid model helps to achieve closer agreement with the measured flow noise, as
184 shown in Fig. 2

185 2.3 Non-dimensional power spectral density

186 The non-dimensional power spectral density, Q_{ND}, of the flow noise is defined as

$$Q_{ND} = \frac{Q(\omega)}{\rho^2 D U^3}, \tag{19}$$

187 where $Q(\omega)$ is the flow noise given by Eq. (10) and D is the cylinder diameter. The non-dimensional
188 power spectral density calculated using the hybrid model (Eqs. (13)-(18)) at different tow speeds
189 are shown in Fig. 4.

190 It can be seen that, the non-dimensional power spectral density for different tow speeds col-
191 lapse to a single curve against the non-dimensional frequency $\omega D/u$. One can therefore obtain
192 the power spectral density at different tow speeds and cylinder diameters using this "single" non-
193 dimensional curve.

194 While developing a new model of turbulent pressure field for axial flow past a solid cylinder, it
195 is assumed that the cylinder is rigid and therefore the pressure field is not altered by the cylinder

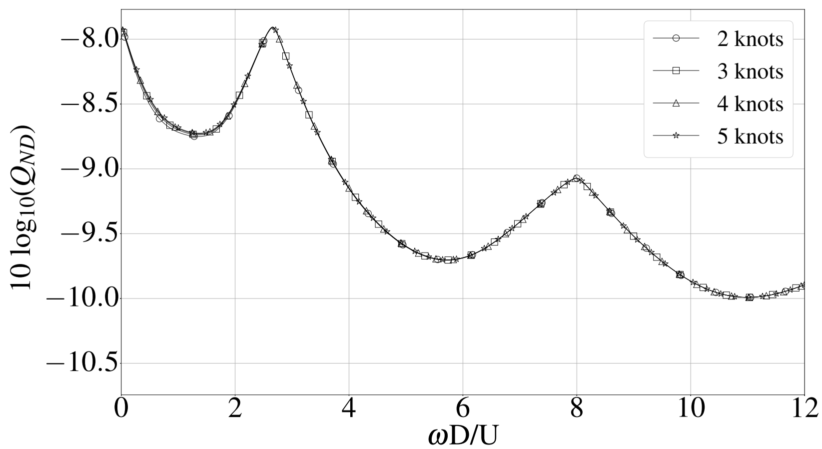

Fig. 4. Non-dimensional power spectral density for different tow speeds using the new hybrid model.

displacement field. However, the cylindrical tube in towed sonar arrays is not rigid and can be assumed to be elastic. The turbulent pressure fluctuation outside the elastic tube, creates vibration inside the tube and in turn generates acoustic waves in the fluid inside the tube. The following section presents a three-dimensional vibroacoustic model of a fluid-filled elastic tube, which is further used with the new hybrid model of the external turbulent pressure excitation to estimate on-axis flow noise.

3 THREE-DIMENSIONAL VIBROACOUSTIC (3D-VA) MODEL OF A FLUID-FILLED ELASTIC TUBE

This section develops a fully-coupled three-dimensional vibroacoustic (3D-VA) model of the fluid-filled elastic tube. A schematic of the fluid-filled tube is shown in Fig. 5. First, the displacement field of the elastic tube is derived from the Navier-Lame equilibrium equation (see Section 3.1) and then the acoustic pressure field inside the tube is derived from the acoustic wave equation (see Section 3.2). The structure (elastic tube) and the fluid (interior fluid) are then coupled with the help of stress and displacement boundary conditions at the interface (see Section 3.3). External pressure excitation is also taken into account in the form of a stress boundary condition on the outer surface of the tube. The boundary conditions, when expressed in terms of the unknown displacement and pressure fields, form a system of linear algebraic equations. The unknown displacement and pressure fields are then calculated by solving this system of equations (see

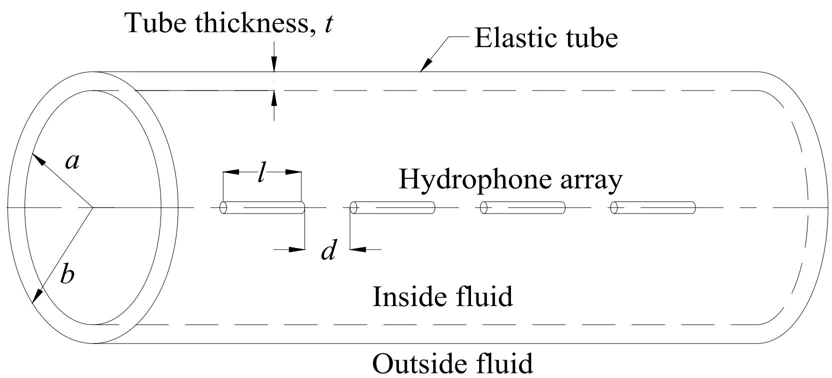

Fig. 5. Fluid filled elastic tube.

Section 3.4).

3.1 The elastic tube displacement and stress fields

This section involves modeling of an elastic tube using the Navier-Lame equilibrium equation in three-dimensional cylindrical coordinates. The Navier-Lame equilibrium equation is given by [15]

$$\mu\nabla^2\mathbf{U}(r,\theta,z,t)+(\lambda+\mu)\boldsymbol{\nabla}\boldsymbol{\nabla}.\mathbf{U}(r,\theta,z,t)=\rho_s\ddot{\mathbf{U}}(r,\theta,z,t), \tag{20}$$

where $\mathbf{U}$ is the displacement vector ($=\{W_e,\Theta_e,U_e\}^T$, W_e represents the radial, Θ_e represents the azimuthal and U_e, the axial displacement fields), λ and μ are the Lame's coefficients, ρ_s is the density of the tube and $\boldsymbol{\nabla}$ is the gradient operator in three dimension given by

$$\boldsymbol{\nabla}=\frac{\partial}{\partial r}\mathbf{e_r}+\frac{1}{r}\frac{\partial}{\partial\theta}\mathbf{e}_{\boldsymbol{\theta}}+\frac{\partial}{\partial z}\mathbf{e_z}. \tag{21}$$

The displacement vector $\mathbf{U}$ may be represented using the Helmholtz decomposition method as

$$\mathbf{U}=\boldsymbol{\nabla}\phi+\boldsymbol{\nabla}\times\boldsymbol{\psi}, \tag{22}$$

where ϕ is a scalar potential and $\boldsymbol{\psi}$ is a vector potential. The scalar and vector potential functions satisfy the Navier-Lame equation for $n = 0$ and for all positive integer values of n. A complete solution to Navier-Lame equation can be obtained as

$$\phi(r,\theta,z,t) = \sum_{n=0}^{\infty} \left[A_1 J_n(\beta_1 r) + A_2 Y_n(\beta_1 r)\right] \left[A_3 \cos(n\theta) + A_4 \sin(n\theta)\right] \mathbf{e}^{i(k_z z - \omega t)}, \tag{23}$$

$$\psi_r(r,\theta,z,t) = \sum_{n=0}^{\infty} \left[C_1 J_{n+1}(\beta_2 r) + C_2 Y_{n+1}(\beta_2 r)\right] \sin(n\theta)\mathbf{e}^{i(k_z z - \omega t)}, \tag{24}$$

$$\psi_\theta(r,\theta,z,t) = \sum_{n=0}^{\infty} - \left[C_1 J_{n+1}(\beta_2 r) + C_2 Y_{n+1}(\beta_2 r)\right] \cos(n\theta)\mathbf{e}^{i(k_z z - \omega t)} \tag{25}$$

and

$$\psi_z(r,\theta,z,t) = \sum_{n=0}^{\infty} \left[B_1 J_n(\beta_2 r) + B_2 Y_n(\beta_2 r)\right] \left[B_3 \cos(n\theta) + B_4 \sin(n\theta)\right] \mathbf{e}^{i(k_z z - \omega t)} \tag{26}$$

In this work, the above expressions are truncated to only $n = 0$ and $n = 1$ terms and further used to compute the elastic tube displacement and stress fields. A detailed derivation of the potential functions are given in Section S1 of the Supplimental material.

3.1.1 Elastic tube displacement components

In this subsection, the displacement components of the elastic tube in radial (W_e), azimuthal (Θ_e) and axial (U_e) directions, are derived. The displacement components are given by Eq. (22).

$$W_e(r,\theta,z,t) = \frac{\partial \phi}{\partial r} + \frac{1}{r}\frac{\partial \psi_z}{\partial \theta} - \frac{\partial \psi_\theta}{\partial z}, \tag{27}$$

$$\Theta_e(r,\theta,z,t) = \frac{1}{r}\frac{\partial \phi}{\partial \theta} + \frac{\partial \psi_r}{\partial z} - \frac{\partial \psi_z}{\partial r} \tag{28}$$

and

$$U_e(r,\theta,z,t) = \frac{\partial \phi}{\partial r} + \frac{1}{r}\frac{\partial \psi_z}{\partial \theta} - \frac{\partial \psi_\theta}{\partial z} \tag{29}$$

Substituting for the scalar (Eq. (23)) and the vector potential (Eqs. (24) - (26)) functions, the radial displacement field is

$$\begin{aligned} W_e(r,\theta,z,t) &= \\ &\mathbf{e}^{i(k_z z-\omega t)}\Big\{\frac{1}{r}[r\beta_1 J_0(r\beta_1)\cos(\theta) - J_1(r\beta_1)(\cos(\theta)+r\beta_1)]E_1 + \frac{1}{r}\sin(\theta)[r\beta_1 J_0(r\beta_1) \\ &- J_1(r\beta_1)]E_2 + \frac{1}{r}[r\beta_1 Y_0(r\beta_1)\cos(\theta) - Y_1(r\beta_1)(\cos(\theta)+r\beta_1)]F_1 + \frac{1}{r}\sin(\theta)[r\beta_1 Y_0(r\beta_1) \\ &- Y_1(r\beta_1)]F_2 + ik_z[J_1(r\beta_2) + J_2(r\beta_2)\cos(\theta)]G_1 + ik_z[J_1(r\beta_2) + J_2(r\beta_2)\cos(\theta)]G_2 \\ &+ [\frac{1}{r}J_1(r\beta_2)\cos(\theta)]H_1 + [\frac{1}{r}Y_1(r\beta_2)\cos(\theta)]H_2 - [\frac{1}{r}J_1(r\beta_2)\sin(\theta)]I_1 - [\frac{1}{r}Y_1(r\beta_2)\sin(\theta)]I_2\Big\}, \end{aligned} \tag{30}$$

where, E_1, E_2, F_1, F_2, G_1, G_2, H_1, H_2, I_1 and I_2 are unknown constants with $E_1 = A_1A_3$, $E_2 = A_1A_4$, $F_1 = A_2A_3$, $F_2 = A_2A_4$, $G_1 = C_1$, $G_2 = C_2$, $H_1 = B_1B_4$, $H_2 = B_2B_4$, $I_1 = B_1B_3$ and

$I_2 = B_2B_3$. The azimuthal displacement field is

$$\begin{aligned}
&\Theta_e(r,\theta,z,t) = \\
&\quad \mathbf{e}^{i(k_z z-\omega t)}\Bigg\{\frac{-1}{r}[J_1(r\beta_1)\sin(\theta)]E_1 + \frac{1}{r}[J_1(r\beta_1)\cos(\theta)]E_2 + \frac{-1}{r}[Y_1(r\beta_1)\sin(\theta)]F_1 \\
&\qquad + \frac{1}{r}[Y_1(r\beta_1)\cos(\theta)]F_2 + [ik_zJ_2(r\beta_2)\sin(\theta)]G_1 + [ik_zY_2(r\beta_2)\sin(\theta)]G_2 \\
&\qquad - \frac{\beta_2\sin(\theta)}{2}[J_0(r\beta_2) - J_2(r\beta_2)]H_1 - \frac{\beta_2\sin(\theta)}{2}[Y_0(r\beta_2) - Y_2(r\beta_2)]H_2 \\
&\qquad + \frac{1}{r}\{-r\beta_2J_0(r\beta_2)\cos(\theta) + J_1(r\beta_2)[r\beta_2 + \cos(\theta)]\}I_1 + \frac{1}{r}\{-r\beta_2Y_0(r\beta_2)\cos(\theta) \\
&\qquad + Y_1(r\beta_2)[r\beta_2 + \cos(\theta)]\}I_2\Bigg\}. \qquad (31)
\end{aligned}$$

The axial displacement field is

$$\begin{aligned}
&U_e(r,\theta,z,t) = \\
&\quad \mathbf{e}^{i(k_z z-\omega t)}\Bigg\{ik_z[J_0(r\beta_1) + J_1(r\beta_1)\cos(\theta)]E_1 + [ik_zJ_1(r\beta_1)\sin(\theta)]E_2 \\
&\qquad + ik_z[Y_0(r\beta_1) + Y_1(r\beta_1)\cos(\theta)]F_1 + [ik_zY_1(r\beta_1)\sin(\theta)]F_2 \\
&\qquad - \beta_2[J_0(r\beta_2) + J_1(r\beta_2)\cos(\theta)]G_1 - \beta_2[Y_0(r\beta_2) + Y_1(r\beta_2)\cos(\theta)]G_2\Bigg\}. \qquad (32)
\end{aligned}$$

The spatio-temporal (r,θ,z,t) displacement field is then transformed to the wavenumber-frequency (r,θ,k_z,ω) domain using the Fourier transform pairs,

$$\hat{G}(r,\theta,k_z,\omega) = \frac{1}{4\pi^2}\int_{-\infty}^{\infty}\int_{-\infty}^{\infty} g(r,\theta,z,t)e^{-i(k_z z-\omega t)}dzdt, \qquad (33)$$

and

$$g(r,\theta,z,t) = \int_{-\infty}^{\infty}\int_{-\infty}^{\infty} \hat{G}(r,\theta,k_z,\omega)\mathbf{e}^{i(k_z z-\omega t)}dk_zd\omega. \qquad (34)$$

The transformed displacement components are given below.

(a) Radial displacement:

$$
\begin{aligned}
\hat{W}_e(r,\theta,k_z,\omega) &= \left\{\frac{-\chi_1}{2}\{2J_1(r\beta_1)+[J_2(r\beta_1)-J_0(r\beta_1)]\cos(\theta)\}\right\}\hat{P}_1(k_z,\omega) \\
&+\left\{\frac{\chi_1}{2}[J_0(r\beta_1)-J_2(r\beta 1)]\sin(\theta)\right\}\hat{P}_2(k_z,\omega)+\left\{\frac{-\chi_1}{2}\{2Y_1(r\beta_1)\right. \\
&\left.+[Y_2(r\beta_1)-Y_0(r\beta_1)]\cos(\theta)\}\right\}\hat{Q}_1(k_z,\omega)+\left\{\frac{\chi_1}{2}[Y_0(r\beta_1)-Y_2(r\beta 1)]\sin(\theta)\right\}\hat{Q}_2(k_z,\omega) \\
&-\left\{\chi_2[J_1(r\beta_2)+J_2(r\beta_2)\cos(\theta)]\right\}\hat{R}_1(k_z,\omega)-\left\{\chi_2[Y_1(r\beta_2)+Y_2(r\beta_2)\cos(\theta)]\right\}\hat{R}_2(k_z,\omega) \\
&+\left\{\frac{1}{r}[J_1(r\beta_2)\cos(\theta)]\right\}\hat{S}_1(k_z,\omega)+\left\{\frac{1}{r}[Y_1(r\beta_2)\cos(\theta)]\right\}\hat{S}_2(k_z,\omega) \\
&+\left\{\frac{1}{r}[J_1(r\beta_2)\sin(\theta)]\right\}\hat{T}_1(k_z,\omega)+\left\{\frac{1}{r}[Y_1(r\beta_2)\sin(\theta)]\right\}\hat{T}_2(k_z,\omega), \quad (35)
\end{aligned}
$$

where $\hat{P}_1(k_z,\omega)$, $\hat{P}_2(k_z,\omega)$, $\hat{Q}_1(k_z,\omega)$, $\hat{Q}_2(k_z,\omega)$, $\hat{R}_1(k_z,\omega)$, $\hat{R}_2(k_z,\omega)$, $\hat{S}_1(k_z,\omega)$, $\hat{S}_2(k_z,\omega)$, $\hat{T}_1(k_z,\omega)$ and $\hat{T}_2(k_z,\omega)$ are the unknown variables and $\chi_1=\frac{\beta_1}{jk_z}$ and $\chi_2=\frac{jk_z}{\beta_2}$.

(b) Azimuthal displacement:

$$
\begin{aligned}
\hat{\Theta}_e(r,\theta,k_z,\omega) &= \left\{\frac{-\chi_1}{r\beta_1}[J_1(r\beta_1)\sin(\theta)]\right\}\hat{P}_1(k_z,\omega)+\left\{\frac{\chi_1}{r\beta_1}[J_1(r\beta_1)\cos(\theta)]\right\}\hat{P}_2(k_z,\omega) \\
&+\left\{\frac{-\chi_1}{r\beta_1}[Y_1(r\beta_1)\sin(\theta)]\right\}\hat{Q}_1(k_z,\omega)+\left\{\frac{\chi_1}{r\beta_1}[Y_1(r\beta_1)\cos(\theta)]\right\}\hat{Q}_2(k_z,\omega) \\
&-\left\{\chi_2 J_2(r\beta_2)\sin(\theta)\right\}\hat{R}_1(k_z,\omega)-\left\{\chi_2 Y_2(r\beta_2)\sin(\theta)\right\}\hat{R}_2(k_z,\omega) \\
&+\left\{\frac{\sin(\theta)}{r}[J_1(r\beta_2)-r\beta_2 J_0(r\beta_2)]\right\}\hat{S}_1(k_z,\omega)+\left\{\frac{\sin(\theta)}{r}[Y_1(r\beta_2)-r\beta_2 Y_0(r\beta_2)]\right\}\hat{S}_2(k_z,\omega) \\
&+\left\{\beta_2 J_0(r\beta_2)\cos(\theta)-\frac{1}{r}\{J_1(r\beta_2)*[r\beta_2+\cos(\theta)]\}\right\}\hat{T}_1(k_z,\omega)
\end{aligned}
$$

$$+\left\{\beta_2 Y_0(r\beta_2)\cos(\theta) - \frac{1}{r}\{Y_1(r\beta_2) * [r\beta_2 + \cos(\theta)]\}\right\}\hat{T}_2(k_z,\omega) \quad (36)$$

(c) Axial displacement:

$$\begin{aligned}\hat{U}_e(r,\theta,k_z,\omega) = &\left\{J_0(r\beta_1) + J_1(r\beta_1)\cos(\theta)\right\}\hat{P}_1(k_z,\omega) + \left\{J_1(r\beta_1)\sin(\theta)\right\}\hat{P}_2(k_z,\omega)\\ &+ \left\{Y_0(r\beta_1) + Y_1(r\beta_1)\cos(\theta)\right\}\hat{Q}_1(k_z,\omega) + \left\{Y_1(r\beta_1)\sin(\theta)\right\}\hat{Q}_2(k_z,\omega)\\ &+ \left\{J_0(r\beta_2) + J_1(r\beta_2)\cos(\theta)\right\}\hat{R}_1(k_z,\omega) + \left\{Y_0(r\beta_2) + Y_1(r\beta_2)\cos(\theta)\right\}\hat{R}_2(k_z,\omega). \quad (37)\end{aligned}$$

The unknown variables in the displacement components, are related to the unknown constants A_1, A_2, A_3, A_4, B_1, B_2, B_3, B_4, C_1 and C_2 in the potential functions as,

$$\hat{P}_1(k_z,\omega) = 2\pi i A_1 A_3 k_z \delta(k+k_z)\delta(\omega-\omega_0), \quad (38)$$

$$\hat{P}_2(k_z,\omega) = 2\pi i A_2 A_3 k_z \delta(k+k_z)\delta(\omega-\omega_0), \quad (39)$$

$$\hat{Q}_1(k_z,\omega) = 2\pi i A_1 A_4 k_z \delta(k+k_z)\delta(\omega-\omega_0), \quad (40)$$

$$\hat{Q}_2(k_z,\omega) = 2\pi i A_2 A_4 k_z \delta(k+k_z)\delta(\omega-\omega_0), \quad (41)$$

$$\hat{R}_1(k_z,\omega) = -2\pi C_1 \beta_1 \delta(k+k_z)\delta(\omega-\omega_0), \quad (42)$$

$$\hat{R}_2(k_z,\omega) = -2\pi C_2 \beta_1 \delta(k+k_z)\delta(\omega-\omega_0), \quad (43)$$

$$\hat{S}_1(k_z,\omega) = 2\pi B_1 B_4 \delta(k+k_z)\delta(\omega-\omega_0), \quad (44)$$

$$\hat{S}_2(k_z,\omega) = 2\pi B_2 B_4 \delta(k+k_z)\delta(\omega-\omega_0), \quad (45)$$

$$\hat{T}_1(k_z,\omega) = -2\pi B_1 B_3 \delta(k+k_z)\delta(\omega-\omega_0), \quad (46)$$

and

$$\hat{T}_2(k_z, \omega) = -2\pi B_2 B_3 \delta(k + k_z)\delta(\omega - \omega_0), \tag{47}$$

where $\delta()$ is the dirac delta function. In the above equations (Eqs. (38)-(47)), two unknown variables can be expressed in terms of other variables as,

$$\hat{Q}_2(k_z, \omega) = \frac{\hat{P}_2(k_z, \omega)\hat{Q}_1(k_z, \omega)}{\hat{P}_1(k_z, \omega)} \text{and} \quad \hat{T}_2(k_z, \omega) = \frac{\hat{S}_2(k_z, \omega)\hat{T}_1(k_z, \omega)}{\hat{S}_1(k_z, \omega)}. \tag{48}$$

Thus, of the ten unknown variables (Eqs. (38)-(47)), present in the displacement fields (Eqs. (35) - (37)), only eight are independent.

3.1.2 Elastic stress components

The elastic tube and the acoustic fluid inside the tube are coupled through displacement and stress boundary conditions. Of all the stress components, only τ_{rr}, $\tau_{r\theta}$, τ_{rz}, and $\tau_{z\theta}$ are of interest to us. These components may be computed using the constitutive relations [15]. They are,

$$\tau_{rr}(r, \theta, z, t) = (\lambda + 2\mu)\frac{\partial W_e}{\partial r} + \frac{\lambda}{r}\left(W_e + \frac{\partial \Theta_e}{\partial \theta}\right) + \lambda \frac{\partial U_e}{\partial z}, \tag{49}$$

$$\tau_{rz}(r, \theta, z, t) = \mu\left(\frac{\partial W_e}{\partial z} + \frac{\partial U_e}{\partial r}\right), \tag{50}$$

$$\tau_{r\theta}(r, \theta, z, t) = \mu\left(\frac{1}{r}\frac{\partial W_e}{\partial \theta} + \frac{\partial \Theta_e}{\partial r} - \frac{\Theta_e}{r}\right), \tag{51}$$

and

$$\tau_{z\theta}(r,\theta,z,t) = \mu\left(\frac{\partial \Theta_e}{\partial z} + \frac{1}{r}\frac{\partial U_e}{\partial \theta}\right). \tag{52}$$

The constitutive relations above are transformed into the frequency - wavenumber ($\omega - k_z$) domain using the Fourier transform pair (Eqs. (33) and (34)). Furthermore, displacement components derived in the previous subsection are substituted to obtain closed form expressions for these stress components (see Eqs. (S.40), (S.44), (S.45) and (S.46) in the supplimental material). A detailed derivation of the stress components using the constitutive relations are given in Section S2 in supplimental material.

3.2 The interior fluid acoustic pressure and displacement fields

The interior fluid is assumed to be confined inside an infinitely long elastic tube. The acoustic wave propagation in the fluid is governed by

$$\nabla^2 p_f(r,\theta,z,t) = \frac{1}{c_a^2}\frac{\partial^2 p_f(r,\theta,z,t)}{\partial t^2}, \tag{53}$$

where p_f is the acoustic pressure, c_a is the speed of sound in the fluid inside the tube and ∇^2 is the Laplacian. In cylindrical coordinates,

$$\nabla^2 = \frac{\partial^2}{\partial r^2} + \frac{1}{r}\frac{\partial}{\partial r} + \frac{1}{r^2}\frac{\partial^2}{\partial \theta^2} + \frac{\partial^2}{\partial z^2}. \tag{54}$$

Assuming a plane wave propagation in the z direction and using a variable separable form for p_f,

$$p_f(r,\theta,z,t) = R(r)\Theta(\theta)e^{j(k_z z - \omega t)}. \tag{55}$$

Substituting Eq. (55) in Eq. (53), and rearranging gives

$$\frac{r^2}{R}\frac{\partial^2 R(r)}{\partial r^2}+\frac{r}{R}\frac{\partial R(r)}{\partial r}+\alpha^2 r^2=-\frac{1}{\Theta}\frac{\partial^2\Theta}{\partial\theta^2}, \tag{56}$$

where $\alpha^2=\frac{\omega^2}{c_a^2}-k_z^2$. For the above equation, only those solutions are valid for which the left hand side and the right hand sides are equal to a positive constant (n^2). Therefore,

$$\frac{r^2}{R}\frac{\partial^2 R(r)}{\partial r^2}+\frac{r}{R}\frac{\partial R(r)}{\partial r}+\alpha^2 r^2=-\frac{1}{\Theta}\frac{\partial^2\Theta}{\partial\theta^2}=n^2. \tag{57}$$

From the above equation, $\Theta(\theta)$ can be obtained by solving

$$\frac{\partial^2\Theta}{\partial\theta^2}+n^2\Theta=0. \tag{58}$$

A general solution to Eq. (58) is

$$\Theta(\theta)=P_{f01}\cos(n\theta)+P_{f02}\sin(n\theta), \tag{59}$$

where P_{f01} and P_{f02} are unknowns. Similarly from Eq. (57), $R(r)$ is governed by,

$$\frac{\partial^2 R}{\partial r^2}+\frac{1}{r}\frac{\partial R}{\partial r}+\left(\alpha^2-\frac{n^2}{r^2}\right)R=0. \tag{60}$$

A general solution to Eq. (60) is

$$R(r)=P_{f03}J_n(\alpha r)+P_{f04}Y_n(\alpha r), \tag{61}$$

where P_{f03} and P_{f04} are unknowns. As $r \to 0$, $Y_n(\alpha r) \to -\infty$, the second term on the right hand side must vanish for all valid pressure fields inside a cylindrical tube. Therefore, $P_{f04} = 0$. Thus, using Eqs. (55), (59) and (61),

$$p_f(r, \theta, z, t) = P_{f03} J_n(\alpha r)[P_{f01} \cos(n\theta) + P_{f02} \sin(n\theta)] e^{j(k_z z - \omega t)} \tag{62}$$

The above equation is valid for $n = 0,1,2,..$etc. A complete solution to the acoustic pressure field may be written as,

$$p_f(r, \theta, z, t) = \sum_{n=0}^{\infty} P_{f03} J_n(\alpha r)[P_{f01} \cos(n\theta) + P_{f02} \sin(n\theta)] e^{j(k_z z - \omega t)} \tag{63}$$

Only $n = 0$ and $n = 1$ terms in Eq. (63) are considered in this work. Further, Eq. (63) is transformed to the frequency-wavenumber ($\omega - k_z$) domain using Eq. (33) and is given by

$$\hat{p}_f(r, \theta, k_z, \omega) = \hat{P}_{f1}(k_z, \omega)[J_0(\alpha r) + J_1(\alpha r) \cos(\theta)] + \hat{P}_{f2}(k_z, \omega) J_1(\alpha r) \sin(\theta), \tag{64}$$

where $\hat{P}_{f1}(k_z, \omega)$ and $\hat{P}_{f2}(k_z, \omega)$ are two unknowns, which are function of the constants P_{f01}, P_{f02} and P_{f03}. They are related as,

$$\hat{P}_{f1}(k_z, \omega) = 2\pi P_{f03} P_{f01} \delta(k + k_z) \delta(\omega - \omega_0) \tag{65}$$

and

$$\hat{P}_{f2}(k_z, \omega) = 2\pi P_{f03} P_{f02} \delta(k + k_z) \delta(\omega - \omega_0). \tag{66}$$

The acoustic particle velocity in the radial, azimuthal and axial directions can be obtained with the help of Euler equation,

$$\boldsymbol{\nabla} p_f(r,\theta,z,t) = -\rho \frac{\partial \mathbf{u}_f(r,\theta,z,t)}{\partial t}, \tag{67}$$

where ∇ is the gradient operator and $\mathbf{u}_f$ is the acoustic particle velocity. The acoustic fluid particle velocity $\mathbf{u}_f$ may be represented as,

$$\mathbf{u}_f(r,\theta,z,t) = u_{fr}(r,\theta,z,t)\mathbf{e_r} + u_{f\theta}(r,\theta,z,t)\mathbf{e}_{\boldsymbol{\theta}} + u_{fz}(r,\theta,z,t)\mathbf{e_z}, \tag{68}$$

where u_{fr}, $u_{f\theta}$ and u_{fz} are the radial, azimuthal and axial components of the fluid particle velocity, respectively. In the above equation, as for the acoustic pressure, a harmonic variation in the form of $\mathbf{e}^{j(k_z z-\omega t)}$ is assumed for the particle velocity. Substituting for $\mathbf{u}_f$ (Eq. (68)) and transforming to the frequency-wavenumber domain, Eq. (67) results

$$\begin{aligned}\frac{\partial \hat{p}_f(r,\theta,k_z,\omega)}{\partial r}\mathbf{e_r} + \frac{1}{r}\frac{\partial \hat{p}_f(r,\theta,k_z,\omega)}{\partial \theta}\mathbf{e}_{\boldsymbol{\theta}} + \frac{\partial \hat{p}_f(r,\theta,k_z,\omega)}{\partial z}\mathbf{e_z} \\ = j\rho\omega \hat{u}_{fr}(r,\theta,k_z,\omega)\mathbf{e_r} + j\rho\omega \hat{u}_{f\theta}(r,\theta,k_z,\omega)\mathbf{e}_{\boldsymbol{\theta}} + j\rho\omega \hat{u}_{fz}(r,\theta,k_z,\omega)\mathbf{e_z}.\end{aligned} \tag{69}$$

3.2.1 Radial component of the fluid particle displacement

Comparing and equating the radial components on the left and right hand sides of Eq. (69) result in

$$\frac{\partial \hat{p}_f(r,\theta,k_z,\omega)}{\partial r} = j\rho\omega \hat{u}_{fr}(r,\theta,k_z,\omega) \tag{70}$$

Substituting for the acoustic pressure $\hat{p}_f(r,\theta,k_z,\omega)$ from Eq. (64) and simplifying yields

$$\hat{u}_{fr}(r,\theta,k_z,\omega) = \frac{1}{j\rho\omega}\left\{\alpha J_0(r\alpha)\cos(\theta) - \frac{J_1(r\alpha)}{r}[r\alpha + \cos(\theta)]\right\}\hat{P}_{f1} + \frac{1}{j\rho\omega}\left\{\frac{\alpha\sin(\theta)}{2}[J_0(r\alpha) - J_2(r\alpha)]\right\}\hat{P}_{f2}. \quad (71)$$

Let U_{fr} be the radial displacement of the fluid particle, defined by

$$U_{fr}(r,\theta,z,t) = \tilde{U}_{fr}(r,\theta)e^{j(k_z z-\omega t)}. \quad (72)$$

In the frequency-wavenumber domain, the fluid particle displacement and velocity in the radial direction are related as

$$\hat{U}_{fr}(r,\theta,k_z,\omega) = \frac{j}{\omega}\hat{u}_{fr}(r,\theta,k_z,\omega). \quad (73)$$

Substituting for $\hat{u}_{fr}(r,\theta,k_z,\omega)$ (Eq. (71)) in the above equation, the radial component of the fluid particle displacement is given by

$$\hat{U}_{fr}(r,\theta,k_z,\omega) = \left\{\frac{1}{r\rho\omega^2}\{r\alpha J_0(r\alpha)\cos(\theta) - J_1(r\alpha)[r\alpha + \cos(\theta)]\}\right\}\hat{P}_{f1} + \left\{\frac{\sin(\theta)}{r\rho\omega^2}[r\alpha J_0(r\alpha) - J_1(r\alpha)]\right\}\hat{P}_{f2}. \quad (74)$$

3.2.2 Azimuthal component of the fluid particle displacement

Comparing and equating the azimuthal components on the left and right hand sides of Eq. (69) result in

$$\frac{1}{r}\frac{\partial \hat{p}_f(r,\theta,k_z,\omega)}{\partial\theta} = j\rho\omega\hat{u}_{f\theta}(r,\theta,k_z,\omega) \tag{75}$$

Substituting for the acoustic pressure $\hat{p}_f(r,\theta,k_z,\omega)$ from Eq. (64) and simplifying yields

$$\hat{u}_{f\theta}(r,\theta,k_z,\omega) = \left\{\frac{1}{r\rho\omega}[j\sin(\theta)J_1(r\alpha)]\right\}\hat{P}_{f1} + \left\{\frac{-1}{r\rho\omega}[j\cos(\theta)J_1(r\alpha)]\right\}\hat{P}_{f2}. \tag{76}$$

Let $U_{f\theta}$ be the azimuthal displacement of the fluid particle defined by

$$U_{f\theta}(r,\theta,z,t) = \tilde{U}_{f\theta}(r,\theta)e^{j(k_z z-\omega t)}. \tag{77}$$

In the frequency-wavenumber domain, the fluid particle displacement and velocity in the azimuthal directions are related as

$$\hat{U}_{f\theta}(r,\theta,k_z,\omega) = \frac{j}{\omega}\hat{u}_{f\theta}(r,\theta,k_z,\omega). \tag{78}$$

Substituting for $\hat{u}_{f\theta}(r,\theta,k_z,\omega)$ (Eq. (76)) in the above equation, the azimuthal component of the fluid particle displacement is given by

$$\hat{U}_{f\theta}(r,\theta,k_z,\omega) = \left\{\frac{-1}{r\rho\omega^2}[J_1(r\alpha)\sin(\theta)]\right\}\hat{P}_{f1} + \left\{\frac{1}{r\rho\omega^2}[J_1(r\alpha)\cos(\theta)]\right\}\hat{P}_{f2}. \tag{79}$$

3.3 Boundary conditions

The field variables derived in the previous subsections involve unknown variables. It is shown in Section 3.1 that the elastic tube displacement (Eqs. (35), (36) and (37)) and stress (Eqs. (49), (50), (51) and (52)) fields have eight unknowns: $\hat{P}_1$, $\hat{P}_2$, $\hat{Q}_1$, $\hat{R}_1$, $\hat{R}_2$, $\hat{S}_1$, $\hat{S}_2$ and $\hat{T}_1$. Section 3.2 shows that the interior fluid pressure (Eq. (64)) and the fluid particle displacement fields (Eqs. (74) and (79)) have two unknowns: $\hat{P}_{f1}$ and $\hat{P}_{f2}$. These ten unknown variables can be calculated with the help of boundary conditions on the inner ($r = a$) and outer ($r = b$) surfaces of the elastic tube. This subsection discusses the ten boundary conditions that are used to compute the ten unknown variables. Note that in the previous subsection, all field variables are expressed in the $r-\theta-k_z-\omega$ domain. These closed form expressions are transformed numerically into the $r-k_\theta-k_z-\omega$ domain using the discrete Fourier transform pair given below before use in the boundary conditions.

$$\hat{G}(r, k_\theta, k_z, \omega) = \sum_{\theta=0}^{N-1} g(r, \theta, k_z, \omega)\mathrm{e}^{-j2\pi k_\theta \theta/N} \tag{80}$$

$$g(r, \theta, k_z, \omega) = \frac{1}{N}\sum_{k_\theta=0}^{N-1} \hat{G}(r, k_\theta, k_z, \omega)\mathrm{e}^{j2\pi k_\theta \theta/N} \tag{81}$$

The ten boundary conditions are given below.

1. On the interior surface of the elastic tube ($r = a$), the radial component of the normal stress τ_{rr} is equal to the negative of the acoustic pressure p_f. In the $k_\theta - k_z - \omega$ domain, this can be written as

$$\hat{\tau}_{rr}(a, k_\theta, k_z, \omega) = -\hat{p}_f(a, k_\theta, k_z, \omega) \tag{82}$$

2. On the exterior surface of the elastic tube ($r = b$), the radial component of the normal stress τ_{rr} is equal to the negative of the external turbulent pressure p_0. In the $k_\theta - k_z - \omega$ domain,

this may be written as

$$\hat{\tau}_{rr}(b, k_\theta, k_z, \omega) = -\hat{p}_0(k_z, \omega) \tag{83}$$

where $\hat{p}_0(k_z, \omega)$ is assumed to be a function of k_z and ω alone and is given by Eq. (18) for the hybrid model. For cases where the external pressure varies with θ, an appropriate pressure spectrum $\hat{p_0}(k_\theta, k_z, \omega)$ must be used.

3. The exterior and interior surfaces of the elastic tube are assumed to be shear-free. Therefore $\tau_{rz}|_{r=a,b} = 0$, $\tau_{r\theta}|_{r=a,b} = 0$ and $\tau_{z\theta}|_{r=a,b} = 0$. In the $k_\theta - k_z - \omega$ domain, this may be written as

$$\hat{\tau}_{rz}(r = a, k_\theta, k_z, \omega) = 0, \tag{84}$$

$$\hat{\tau}_{rz}(r = b, k_\theta, k_z, \omega) = 0, \tag{85}$$

$$\hat{\tau}_{r\theta}(r = a, k_\theta, k_z, \omega) = 0, \tag{86}$$

$$\hat{\tau}_{r\theta}(r = b, k_\theta, k_z, \omega) = 0, \tag{87}$$

$$\hat{\tau}_{z\theta}(r = a, k_\theta, k_z, \omega) = 0, \tag{88}$$

and

$$\hat{\tau}_{z\theta}(r = b, k_\theta, k_z, \omega) = 0. \tag{89}$$

4. The radial (W_e) and azimuthal (Θ_e) components of the elastic tube displacements on the interior surface ($r = a$) must be equal to the respective fluid particle displacement (U_{fr} and $U_{f\theta}$) at $r = a$. In the $k_\theta - k_z - \omega$ domain, this may be written as

$$\hat{U}_{fr}(a, k_\theta, k_z, \omega) = \hat{W}_e(a, k_\theta, k_z, \omega) \tag{90}$$

and

$$\hat{U}_{f\theta}(a, k_\theta, k_z, \omega) = \hat{\Theta}_e(a, k_\theta, k_z, \omega). \tag{91}$$

The expressions for the acoustic pressure, the fluid and the elastic tube displacement components, and the elastic tube stress components derived in the previous subsections are substituted in the above boundary conditions. The resulting equations are given in detail in Section S3 in the supplimental material.

3.4 Solution methodology

Previous section discussed the boundary conditions associated with the elastic tube displacements and the acoustic pressure variations inside and outside the elastic tube. These boundary conditions result in ten equations involving twelve unknown variables (see section S3 in the supplimental material). Of the twelve unknown variables, only ten are independent. A further simplification of the boundary condition to include only the ten independent unknowns are presented in section S4 in supplimental material. The resulting system of algebraic equations may be represented in a matrix form,

$$\mathbf{A}(r, k_\theta, k_z, \omega)\,\mathbf{x} = \mathbf{b}(r, k_\theta, k_z, \omega), \tag{92}$$

where $\mathbf{A}$ is the coefficient matrix of order 10×10, $\mathbf{x}$ is the unknown variable vector of order 10×1 and $\mathbf{b}$ is the constant vector of order 10×1. A detailed representation of $\mathbf{A}$, $\mathbf{x}$ and $\mathbf{b}$ are given in section S4 in the supplimental material. Eq. (92) is solved numerically for the unknown variable vector $\mathbf{x}$ and the solution is used to calculate the interior acoustic pressure field $\hat{p}_f(r, k_\theta, k_z, \omega)$. The acoustic pressure field $\hat{p}_f(r, k_\theta, k_z, \omega)$ is further used to compute (a) azimuthal variation in the acoustic pressure field inside the elastic tube, (b) on-axis flow noise spectrum, and (c) on-axis flow noise.

3.4.1 Azimuthal variation in the interior acoustic pressure field

The interior acoustic pressure field $\hat{p}_f(r, k_\theta, k_z, \omega)$ is first multiplied with the square of the hydrophone response function $H(k_z)$ (Eq. (11)) and then integrated over the entire axial wavenumber domain to get

$$Q(r = a, k_\theta, f) = 4\pi \int_{-\infty}^{\infty} \hat{p}_f(r = a, \theta, k_z, \omega)|H(k_z)|^2 dk_z. \tag{93}$$

The factor 4π is used to account for the negative frequency and radian frequency measure [8, 9, 12]. The azimuthal variation in $Q(r = a, \theta, f)$ may be computed using the inverse Fourier transform,

$$Q(r = a, \theta, f) = \frac{1}{N} \sum_{k_\theta=0}^{N-1} Q(r = a, k_\theta, f) e^{j2\pi k_\theta \theta / N}. \tag{94}$$

The azimuthal variation in acoustic pressure level at the tube inner surface is computed using

$$SPL(r = a, \theta, f) = 10 \ \log_{10} \left(\frac{|Q(a, \theta, f)|}{p_{ref}^2} \right), \tag{95}$$

where $p_{ref} = 1 \mu Pa$ is the reference acoustic pressure in water.

3.4.2 On-axis flow noise spectrum level

The acoustic pressure field $\hat{p}_f(r, k_\theta, k_z, \omega)$ is integrated over the azimuthal wavenumbers to obtain the on-axis flow noise spectrum as a function of frequency (ω) and axial wavenumber (k_z).

$$\hat{p}_f(r = 0, k_z, \omega) = \int_{-\infty}^{\infty} \hat{p}_f(r = 0, k_\theta, k_z, \omega) dk_\theta. \tag{96}$$

The on-axis flow noise spectrum level can be calculated by

$$SPL(r=0,k_z,\omega) = 10\ \log_{10}\left(\frac{|\hat{p}_f(r=0,k_z,\omega)|}{p_{ref}^2}\right). \tag{97}$$

3.4.3 On-axis flow noise

First, the on-axis flow noise spectrum is computed using Eq. (96). It is further multiplied with the square of the hydrophone response function $H(k_z)$ (Eq. (11)) and integrated over the axial wavenumbers k_z to obtain on-axis flow noise $Q(r=0,f)$. Thus,

$$Q(r=0,f) = 4\pi \int_{-\infty}^{\infty} \hat{p}_f(r=0,k_z,\omega)|H(k_z)|^2 dk_z. \tag{98}$$

The on-axis flow noise level can be computed using

$$SPL(r=0,f) = 10\ \log_{10}\left(\frac{|Q(r=0,f)|}{p_{ref}^2}\right). \tag{99}$$

4 RESULTS AND DISCUSSIONS

Previous sections discussed the development of a fully-coupled three-dimensional vibroacoustic (3D-VA) model of a fluid-filled elastic tube under external pressure excitations. In this section, the 3D-VA model is used to estimate the interior acoustic pressure field and flow noise in towed sonar arrays. Section 4.1 presents the interior acoustic pressure field for azimuthally varying external pressure excitation over the fluid-filled elastic tube. Section 4.2 discusses the on-axis flow noise spectrum due to an external turbulent pressure excitation. External turbulent pressure excitation is computed using the hybrid model developed in this work (see Section 2). The results are then compared with those obtained using the tube transfer function [9] and the axisymmetric vibroacoustic [11, 16] models available in the literature. Section 4.3 presents the on-axis flow noise computed using the 3D-VA model and further compares the results with those predicted using tube transfer function [9] and the axisymmetric [11] models. Further, Section 4.4 discusses the flow noise variation for various elastic tube diameters at different tow speeds.

4.1 Interior acoustic pressure field for azimuthally varying external excitation

The developed 3D-VA model of the fluid-filled elastic tube is initially tested with an exterior harmonic pressure excitation that has a known azimuthal variation. Results for two different external pressure excitation are presented here : (a) $\hat{p}_0(\theta, k_z) = \sin(\theta)$ (see Fig. 6) and (b) $\hat{p}_0(\theta, k_z) = \cos(\theta)$ (see Fig. 7).

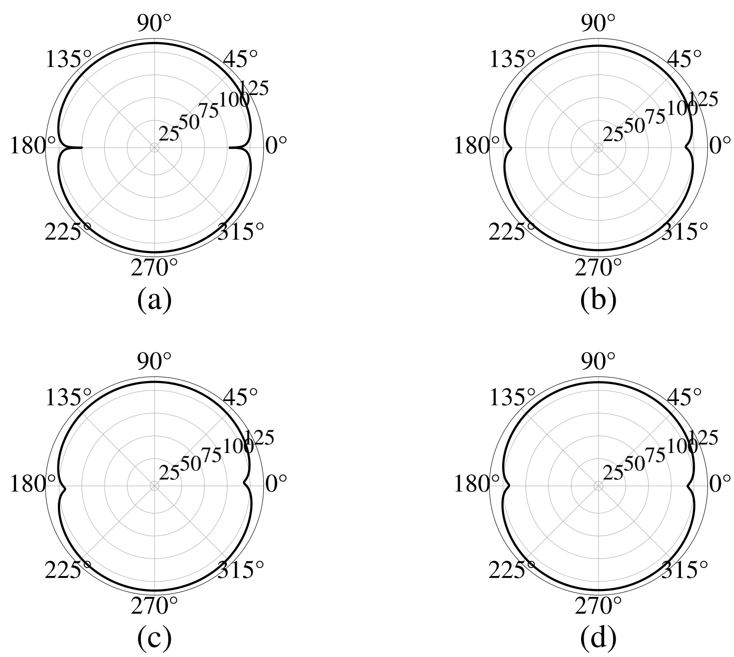

Fig. 6. (a): Azimuthal variation in the exterior pressure field $\hat{p}_0(\theta, k_z) = \sin(\theta)$. (b), (c) and (d): Azimuthal variation in the interior pressure field ($r = a$) at 10 Hz, 100 Hz and 1000 Hz, respectively, for $\hat{p}_0(\theta, k_z) = \sin(\theta)$.

Fig. 6(a) shows the azimuthal variation in the acoustic pressure (see Eqs. (93) - (95) with $\hat{p}_f$ being replaced with $\sin(\theta)$) at the outer surface of the elastic tube. Figs. 6(b) - 6(d) shows the resulting azimuthal variation in the acoustic pressure at the inner surface (r=a) of the elastic tube for (b): 10 Hz, (c) 100 Hz and (d) 1000 Hz. Fig. 7 shows similar results for $\hat{p}_0(\theta, k_z) = \cos(\theta)$. The Figs. 6 and 7 confirms that the 3D-VA model accurately captures the azimuthal variation (restricted

402 to $n = 0$ and $n = 1$) in the external pressure excitation.

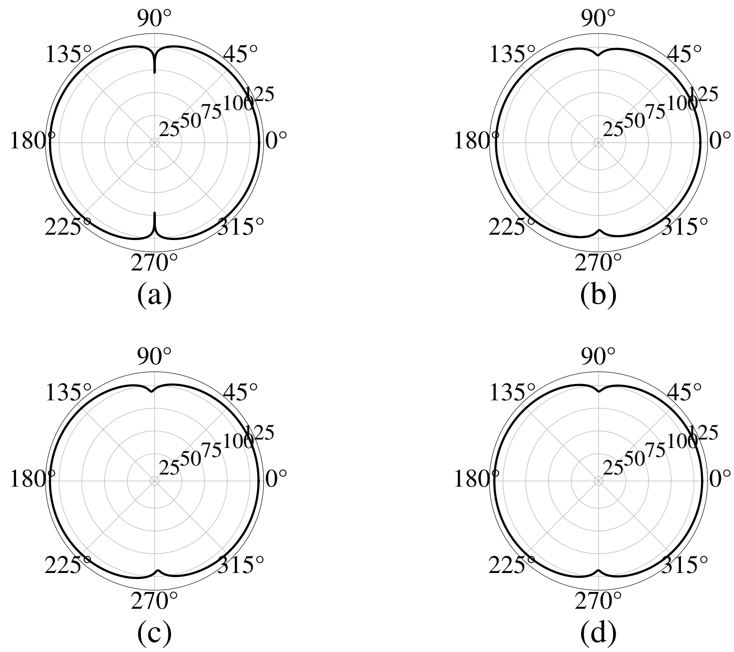

Fig. 7. (a): Azimuthal variation in the exterior pressure field $\hat{p}_0(\theta, k_z) = \cos(\theta)$. (b), (c) and (d): Azimuthal variation in the interior pressure field ($r = a$) at 10 Hz, 100 Hz and 1000 Hz, respectively, for $\hat{p}_0(\theta, k_z) = \cos(\theta)$.

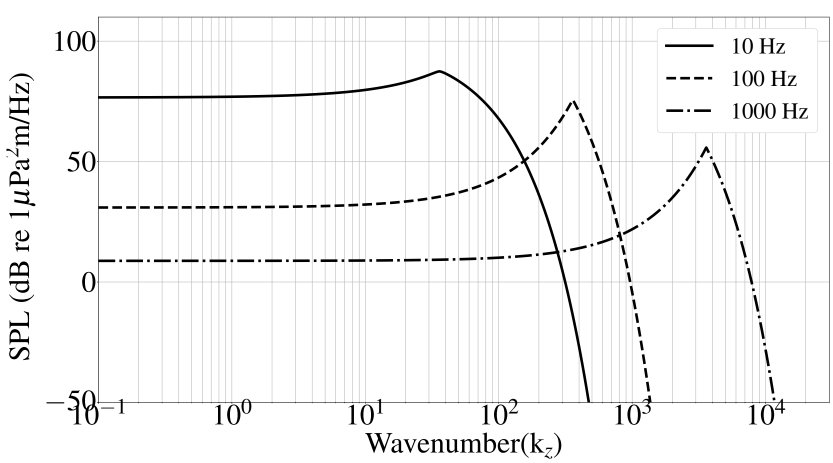

Fig. 8. The external turbulent pressure spectrum level computed using the hybrid model (Eq. (18)).

Table 1. The elastic tube, interior fluid and the hydrophone array parameters used for estimation of flow noise inside the cylinder

Property	**Values**
Tube diameter (m)	0.04
Tube thickness (m)	0.005
Tow speed/Flow velocity (knots)	5
Number of hydrophones	50
Length of hydrophone (m)	0.05
Hydrophone spacing (m)	0.25
Exterior fluid density (kg/m^3)	1000
Interior fluid density (kg/m^3)	800
Reference pressure (μ Pa)	1

4.2 On-axis flow noise spectrum level for external turbulent pressure excitation

This section presents on-axis flow noise spectrum when the elastic tube is excited by an external turbulent pressure field. The external turbulent pressure field (see Fig. 8) is computed using the hybrid model (Eq. (18)). Further, the 3D-VA model is used to calculate the on-axis flow noise spectrum (see Eqs. (96) and (97)). This flow noise spectrum is compared with that computed using the tube transfer function model [9] (see Fig. 9) and the axisymmetric model [11] (see Fig. 10). The elastic tube, inside fluid, and hydrophone array parameters used for computation are listed in Table 1. It can be seen from Figs. 9 and 10 that the on-axis acoustic pressure computed using the 3D-VA model follows the external turbulent pressure excitation given in Fig. 8 - gradually increasing up to and peaking at the convective wavenumber ($u_c = \omega/k_c$), and decreasing exponentially beyond. Thus, the flow noise inside the tube is dominated by the contribution from wavenumbers less than the convective wavenumber.

In the tube transfer function model (Fig. 9) and the axisymmetric model (Fig. 10) predictions, the peak occurs at a lower wavenumber than the convective wavenumber. For example, at 10 Hz, the peak occurs at 1.58 rad/m in the tube transfer function model and at 1.56 rad/m in the axisymmetric model. Note that the convective wavenumber at 10 Hz for 5 knots is $k_c = 35.93$ rad/m. This

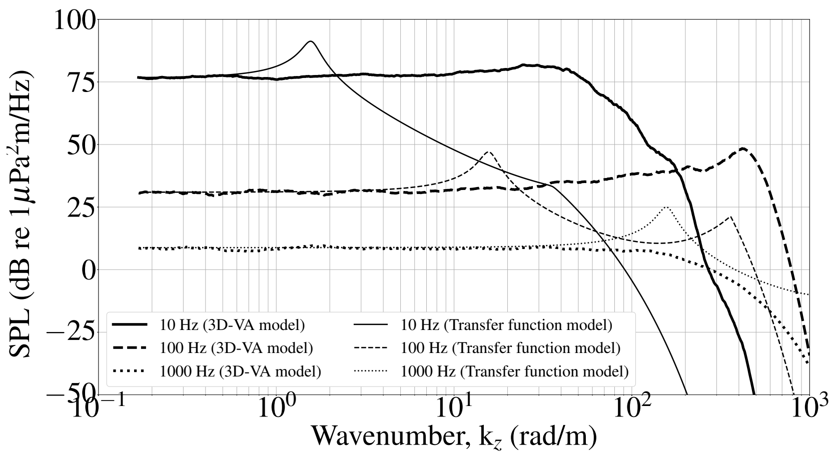

Fig. 9. Comparison of on-axis flow noise spectrum level due to a turbulent pressure excitation computed using the 3D-VA model and the tube transfer function model [9].

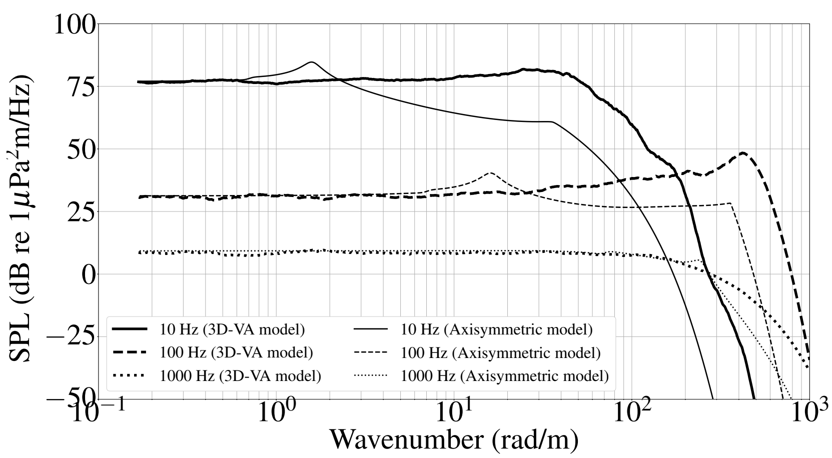

Fig. 10. Comparison of on-axis flow noise spectrum level due to a turbulent pressure excitation computed using the 3D-VA model and the axisymmetric model [11].

smaller wavenumber where the first peak occurs in the transfer function and the axisymmetric models corresponds to the breathing mode wavenumber, k_b, of the elastic tube given by [9]

$$k_b^2 = 2\rho_0\omega^2 R/Et. \tag{100}$$

In Eq. (100), ρ_0 is the density of the inside fluid, R is the outer radius of the elastic tube, E is the Young's modulus of the tube and t is the thickness of the tube. The tube transfer function model and the axisymmetric model consider only the breathing mode ($n = 0$) variations while

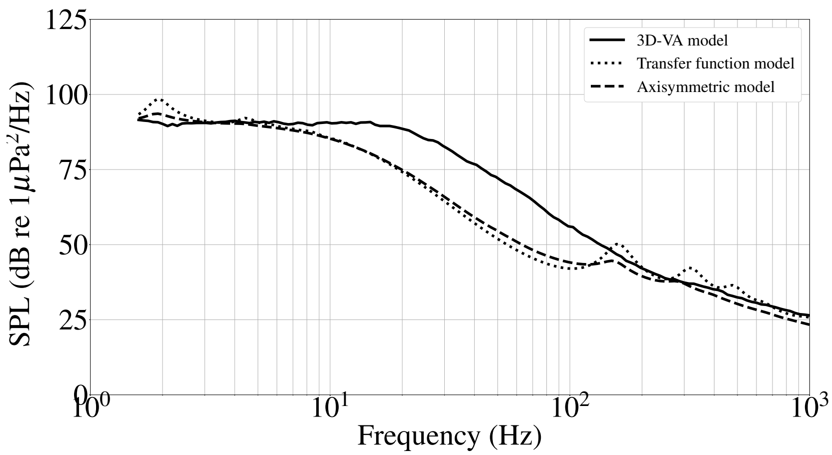

Fig. 11. The on-axis flow noise due to the turbulent pressure excitation computed using the 3D-VA model, the tube transfer function model [9] and the axisymmetric model [11].

modeling the fluid-filled elastic tube. The present 3D-VA model considers both $n = 0$ (breathing) and $n = 1$ (first order) variations in the solid and fluid displacement fields. The absence of peaks at the breathing wavenumber in the present 3D-VA model indeed demonstrates a cumulative effect of including both $n = 0$ and $n = 1$ order terms in the fully-coupled vibroacoustic formulation. The same is the reason for the difference in the flow noise spectrum between the 3D-VA model and the other models beyond the breathing wavenumber.

4.3 On-axis flow noise for external turbulent pressure excitation

This section presents the flow noise as heard by the hydrophones placed inside the fluid-filled elastic tube. The flow noise is computed using Eqs. (98) and (99). Note that flow noise at a given frequency can be obtained by integrating the corresponding flow noise spectrum (Figs. 9 and 10) over the wavenumber. Fig. 11 shows the variation in flow noise with frequency, computed using the 3D-VA model. It also depicts the flow noise predicted by the tube transfer function [9] and the axisymmetric [11] models. Note that in all cases, the external turbulent pressure excitation is given by Eq. (18) (the hybrid model). The elastic tube, interior fluid and hydrophone parameters are given in Table 1. It can be seen from Fig. 11 that the flow noise decreases with frequency. This decrease is attributed to the reduction in the external turbulent pressure excitation with frequency as shown in Fig. 8. As mentioned earlier, the 3D-VA model considers both $n = 0$ (breathing) and $n = 1$ variation in the acoustic pressure field. This results in a better flow noise prediction than the

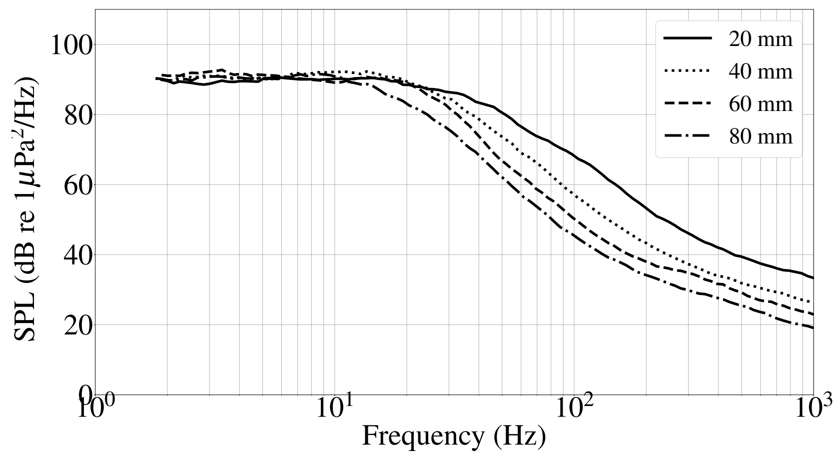

Fig. 12. Comparison of on-axis flow noise estimated using 3D-VA model, due to a turbulent pressure excitation at 5 knots over an elastic tube for different diameters.

transfer function and axisymmetric models, where only the $n = 0$ or the breathing wavenumber is considered. The transfer function and the axisymmetric models underpredict the flow noise in the mid frequency range (10 Hz - 200 Hz). It is evident from Figs. 9 and 10 that the difference between the 3D-VA and other models is not significant as the frequency increases. For that reason, the flow noise predictions (Fig. 11) by the three models are quite close to each other at high frequencies (beyond $\sim$ 200 Hz).

4.4 On-axis flow noise for different tube diameters and tow speeds

In this section, the on-axis flow noise (Eqs. (98) and (99)) is computed for different elastic tube diameters at different tow speeds. Fig. 12 shows the comparison of on-axis flow noise estimated for different elastic tube diameters at 5 knots and Fig. 13 shows the variation in the flow noise for a tube of 40 mm diameter at different tow speeds. The variation in flow noise is attributed to the changes in external turbulent pressure excitation with tube diameters and tow speeds, as shown in Fig. 4 (the non-dimensional plot). It was shown in Fig. 4 that an increase in diameter or a decrease in tow speed results in a reduction in the non-dimensional power spectral density. This leads to a decrease in on-axis flow noise inside the fluid-filled elastic tube with increasing tube diameter (Fig. 12) or decreasing tow speeds (Fig. 13).

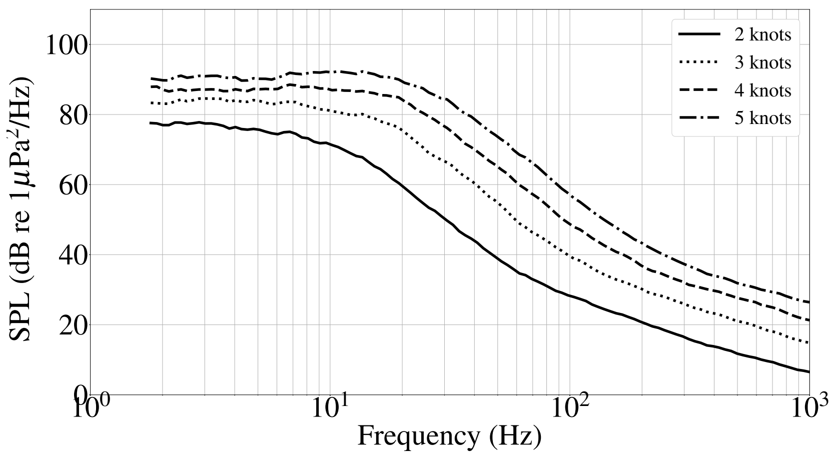

Fig. 13. Comparison of on-axis flow noise estimated using 3D-VA model, due to a turbulent pressure excitation over an elastic tube of 40 mm diameter at different tow speeds.

5 CONCLUSIONS

A new semi-empirical (hybrid) model is developed for estimating the wavenumber-frequency spectrum of turbulent pressure for an axial flow past a solid cylinder. The hybrid model is derived using insights from different turbulent pressure semi-empirical models (Chase [4] and Frendi *et al.* [5]) and the experimental results of Unnikrishnan *et al.* [2]. The hybrid model predictions are found to be superior to the existing semi-empirical models and compares reasonably well with available experimental results.

A fully-coupled three-dimensional vibroacoustic model (3D-VA model) is developed for computing the pressure field inside the fluid-filled elastic tube due to external turbulent pressure excitations. In this 3D-VA model, the structure (elastic tube) is modeled using the Navier-Lame equilibrium equations, and the fluid inside the tube is modeled using the acoustic wave equation. The 3D-VA model is first tested for an exterior harmonic pressure excitation having a known azimuthal variation. The interior pressure field is found to follow the same azimuthal variation as that of the external excitation.

Next, the 3D-VA model is used in conjunction with the hybrid model of the turbulent pressure spectrum to find the on-axis flow noise. The results are then compared with the on-axis flow noise estimated using an existing transfer function model [9] and an axisymmetric vibroacoustic model. The transfer function and the axisymmetric models consider only the breathing mode ($n = 0$) of the elastic tube, but the 3D-VA model considers both $n = 0$ (breathing) and $n = 1$ (first order) variations in modeling the elastic tube and the fluid inside the tube. Consequently, it is observed that the two other models underpredict the flow noise compared to the 3D-VA model.

The on-axis flow noise is then estimated for different elastic tube diameters and tow speeds. At low frequencies, an increase in the tube diameter causes negligible variation in flow noise, but at higher frequencies, the flow noise decreases with increase in the tube diameter. When the tow speed is increased, the flow noise is found to increase at all frequencies.

ACKNOWLEDGEMENTS

This research was supported by the Defence Research and Development Organisation, India. The authors express their sincere gratitude to Dr. Ganesh Natarajan and Dr. Pramod Kuntikana (Indian Institute of Technology Palakkad) for their invaluable support and guidance throughout this investigation. Special thanks also go to Dr. T. Santhanakrishnan, Mr. Sameer Abdul Azeez, Mr. Jineesh George, Mr. Samuel Theophilus, and Mr. Anshath Hussain (Naval Physical & Oceanographic Laboratory) for their invaluable feedback and assistance with this project. We express our gratitude to Prof. A. Seshadri Sekhar, Director of the Indian Institute of Technology Palakkad and Dr. Duvvuri Seshagiri, OS and Director of the Naval Physical & Oceanographic Laboratory, for their support in enabling this collaborative research.

REFERENCES

[1] Gopi, S., Felix, V. P., Sebastian, S., Pallayil, V., and Kuselan, S., 2010, "In-situ non-acoustic noise measurement system for towed hydrophone array," In 2010 IEEE Instrumentation & Measurement Technology Conference Proceedings, pp. 913–916.

[2] Unnikrishnan, K. C., Pallayil, V., Chitre, M. A., and Kuselan, S., 2011, "Estimated flow noise levels due to a thin line digital towed array," In OCEANS 2011 IEEE - Spain, pp. 1–4.

[3] Corcos, G. M., 1963, "Resolution of Pressure in Turbulence," *The Journal of the Acoustical Society of America,* **35**(2), 02, pp. 192–199.

[4] Chase, D., 1981, "Further modeling of turbulent wall pressure on a cylinder and its scaling

with diameter," *NASA STI/Recon Technical Report N,* **82**, p. 29561.

[5] Frendi, A., and Zhang, M., 2020, "A New Turbulent Wall-Pressure Fluctuation Model for Fluid–Structure Interaction," *Journal of Vibration and Acoustics,* **142**(2), 01, p. 021018.

[6] Goody, M., 2004, "Empirical spectral model of surface pressure fluctuations," *AIAA Journal,* **42**(9), pp. 1788–1794.

[7] Francis, R., Ebenezer, D. D., Bhattacharyya, S. K., and Sharma, R., 2023, "Estimation of wavenumber–frequency spectra of wall pressure due to turbulent flow over a flat plate using large-eddy simulation," *Physics of Fluids,* **35**(6), 06, p. 065110.

[8] Carpenter, A., and Kewley, D., 1983, "Investigation of low wavenumber turbulent boundary layer pressure fluctuations on long flexible cylinders," In Eighth Australasian Fluid Mechanics Conference, Vol. 28, 9A.

[9] Knight, A., 1996, "Flow noise calculations for extended hydrophones in fluid- and solid-filled towed arrays," *The Journal of the Acoustical Society of America,* **100**(1), 07, pp. 245–251.

[10] Karthik, K., Jeyakumar, S., and Sebastin, J. S., 2021, "Numerical prediction of flow noise levels on towed sonar array," *Proceedings of the Institution of Mechanical Engineers, Part M: Journal of Engineering for the Maritime Environment,* **235**(2), pp. 600–606.

[11] Jineesh, G., and Ebenezer, D. D., 2013, "Response of a linear array of hydrophones to flow-induced noise," In Acoustics, New Delhi - India, pp. 1–6.

[12] Kuttan Chandrika, U., Pallayil, V., Lim, K. M., and Chew, C. H., 2014, "Flow noise response of a diaphragm based fibre laser hydrophone array," *Ocean Engineering,* **91**, pp. 235–242.

[13] Huang, C., Li, H., and Li, N., 2020, "Flow noise spectrum analysis for vertical line array during descent in deep water," *Journal of Theoretical and Computational Acoustics,* **28**(04), p. 2050022.

[14] Jordan, S. A., 2014, "On the Axisymmetric Turbulent Boundary Layer Growth Along Long Thin Circular Cylinders," *Journal of Fluids Engineering,* **136**(5), 03, p. 051202.

[15] Sadd, M., 2014, *Elasticity: Theory, applications, and numerics, third edition* 01.

[16] Sekharipuram Sekar, R., Natarajan, G., Kuntikana, P., and Akkoorath Mana, A., 2024, "An axisymmetric model for predicting turbulent flow noise in towed sonar arrays," In Proceedings

of the 30th International Congress on Sound and Vibration, pp. 1–8.

LIST OF FIGURES

1 Comparison of flow noise predicted by Chase [4] and Frendi [5] models with the experimental results [2] at different tow speeds. 8

2 A comparison of flow noise predicted by the hybrid model, the Chase model [4] and Frendi model [5] with that measured from experiments [2] at different tow speeds. . . 11

3 A comparison of the turbulent pressure spectrum $\hat{p}_0(k_z, \omega)$ given by the hybrid model (Eq. (18)), Chase (Eq. (1)) and Frendi (Eq. (9)) model at 2 knots. 12

4 Non-dimensional power spectral density for different tow speeds using the new hybrid model. 13

5 Fluid filled elastic tube. 14

6 (a): Azimuthal variation in the exterior pressure field $\hat{p}_0(\theta, k_z) = \sin(\theta)$. (b), (c) and (d): Azimuthal variation in the interior pressure field $(r = a)$ at 10 Hz, 100 Hz and 1000 Hz, respectively, for $\hat{p}_0(\theta, k_z) = \sin(\theta)$. 32

7 (a): Azimuthal variation in the exterior pressure field $\hat{p}_0(\theta, k_z) = \cos(\theta)$. (b), (c) and (d): Azimuthal variation in the interior pressure field $(r = a)$ at 10 Hz, 100 Hz and 1000 Hz, respectively, for $\hat{p}_0(\theta, k_z) = \cos(\theta)$. 33

8 The external turbulent pressure spectrum level computed using the hybrid model (Eq. (18)). 33

9 Comparison of on-axis flow noise spectrum level due to a turbulent pressure excitation computed using the 3D-VA model and the tube transfer function model [9]. . . 35

10 Comparison of on-axis flow noise spectrum level due to a turbulent pressure excitation computed using the 3D-VA model and the axisymmetric model [11]. 35

11 The on-axis flow noise due to the turbulent pressure excitation computed using the 3D-VA model, the tube transfer function model [9] and the axisymmetric model [11]. 36

12 Comparison of on-axis flow noise estimated using 3D-VA model, due to a turbulent pressure excitation at 5 knots over an elastic tube for different diameters. 37

13 Comparison of on-axis flow noise estimated using 3D-VA model, due to a turbulent pressure excitation over an elastic tube of 40 mm diameter at different tow speeds. . 38

LIST OF TABLES

1 The elastic tube, interior fluid and the hydrophone array parameters used for estimation of flow noise inside the cylinder 34